Review Article
X-ray fluorescence imaging of metals and metalloids in biological systems

Run Zhang[1], Li Li[1], Yasmina Sultanbawa[2], Zhi Ping Xu[1]

[1]Australian Institute for Bioengineering and Nanotechnology, The University of Queensland, St Lucia, QLD 4072, Australia; [2]Centre for Nutrition and Food Sciences, Queensland Alliance for Agriculture and Food Innovation, The University of Queensland, Coopers Plains, QLD 4072, Australia

Abstract: Metals and metalloids play fundamental roles in many physiological processes in biological systems, but imbalance of these elements in the body may cause many diseases, such as Parkinson's disease, Alzheimer's disease, and even cancers. Thus, to better understand the metallome in health and disease, quantitative determination of their localization, concentration, speciation, and related metabolism at cellular or subcellular levels is of great importance. X-ray fluorescence (XRF) imaging, as a new generation of analytical technique, has been reported as an ideal tool to quantitatively map multiple metals and metalloids in tissues with reasonable sensitivity, specificity, and resolution. In the current review, we have introduced the general concept of XRF imaging technique, reviewed the recent advances using XRF imaging to investigate toxicology of metals and metalloids in life science, and discussed the roles of metals and metalloids in various diseases, including cancers and neurodegenerative diseases. We believe that future research on revealing the roles of metals and metalloids in biological systems will directly benefit from the important breakthroughs in developing XRF imaging techniques.

Keywords: X-ray fluorescence, metals and metalloids, fluorescence imaging, toxicology, diseases

Introduction

In this review paper, metals and metalloids may mean the metal ions and any available forms, such as metal-oxygen anions and metal ion-ligand coordinates, and sometimes not strictly, mean some non-metals, such as As, P, Cl etc. that XRF is able to detect, for simplicity in description.

Metals and metalloids in biological systems

Metals and metalloids perform critical roles in fundamental processes required for all biological species, including osmotic regulation, catalysis, metabolism, biomineralization, and signalling [1, 2]. Most biological organisms do not only contain abundant alkali and alkaline earth metals but also store and transport transition metals and metalloids to provide appropriate levels for metalloproteins or cofactors, and protect themselves against the toxic effects [3-5]. In general, the concentration of transition metals and metalloids, such as zinc (Zn), copper (Cu), manganese (Mn), iron (Fe), nickel (Ni), chromium (Cr), arsenate (As) and cadmium (Cd), is much lower than that of alkali and alkaline earth metals [6]. Nevertheless, metalloproteins and metal cofactors are found almost in all plants, animals, and microorganisms [1, 7, 8].

In living systems, the normal concentration range for each metal or metalloid is narrow (**Table 1**) [9], while both deficiency and excess of these elements can cause pathological changes [8, 10]. For example, the World Health Organization (WHO) and the Food and Agricultural Administration (FAA) suggest that the population mean intake of Cu should not exceed 10-12 mg per day for adults [11]. The deficiency of Cu in the human body would increase the risk associated with developing coronary heart disease [12-14], while the Menke's disease, Alzheimer's disease, Parkinson's disease, Wilson's disease, and Occipital Horn Syndrome are implicated with the excessive amount of Cu uptake and excretion [13, 15-17]. Since metals and metalloids in liv-

Table 1. Average relative abundance of selected elements in earth's crust and mammalian blood plasma [6, 9]

Conc. of Metals	Ni	Cd	Zn	As	Cu	Mn	Fe	Cr	Na	K	Ca
Crust (ppm)	75	0.2	70	1.5	55	950	5×10^4	100	3×10^4	3×10^4	4×10^4
Blood (µM)	0.04	-	17	-	8-24	0.1	22	0.5	1×10^5	4×10^3	2×10^3

Table 2. Comparison of the microanalytical techniques [23-31, 33-35]

| Analytical technique	Detection limit	Spatial resolution	Analytical depth (mm)	Quantification	Ref
MS	0.01 mg/g	15-50 mm	200	Semiquantitative	[23, 24]
Fluorescence	pM to nM	2-3 mm (in vivo), 0.2-0.5 mm (in vitro)	< 1 cm	Quantitative/semiquantitative	[25, 26]
PET	High pM	1-2 mm	No limit	Semiquantitative	[27-29]
SPECT	Low nM	15-20 mm	No limit	Semiquantitative	[28, 29]
MRI	mM to low µM	25-100 mm	No limit	Semiquantitative	[30, 31]
XRF	0.1-1 mg/g	0.03-0.2 mm	> 100	Quantitative	[33-35]
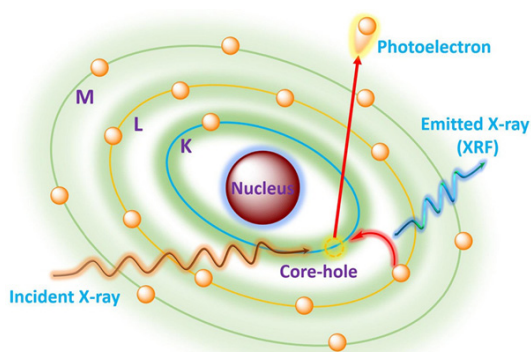
Figure 1. Basic principle of X-ray fluorescence.

ing systems are essential, researchers in chemistry, biology, and medicine have been attracted to relate their excess or deficiency in living systems to specific diseases [9, 16]. Therefore, understanding of the localization, speciation, and metabolism of these metals and metalloids at molecular level is of great importance.

It is well known that the metals and metalloids in biological samples exist in different forms, such as free ions, metalloproteins or cofactors formed through complexation [7-9], and are not homogenously distributed in biological cells and tissues [18]. As a consequence, *in-situ* spatiotemporal analysis of their formation, concentration and distribution in living systems remains a great challenge [4, 5]. Up to now, a variety of methods have been developed and used to quantitatively determine these metals and metalloids in biological samples. Among these approaches, *in-situ* imaging technique

has been reported as one of the most promising methods for the study of metals in living systems due to its capability of high spatial and temporal resolution [1, 16, 19]. Recently, several imaging techniques have been proposed to visualize the location and determine the concentration level of specific metals in biological samples [16, 20-22]. **Table 2** illustrates an overview of the most important imaging-based microanalytical techniques. Imaging mass spectrometry (IMS) technology is used to record spatial and temporal resolution of metals and metalloids in biological samples at the cellular and/or subcellular levels [5, 23, 24]. Another imaging technology that permits the mapping of a specific metal in living specimens with high sensitivity and spatiotemporal resolution involves utilization of fluorescent biosensors [4, 16, 25, 26]. When the intracellular biosensor interaction with specific metals or metalloids, the location and level of these elements will be immediately recorded as the changes in fluorescence output, either through an intensity increase or an energy shift of the emitted light [25, 26]. Other imaging techniques, such as magnetic resonance imaging (MRI), positron emission tomography (PET), and single-photon emission computed tomography (SPECT), have also been developed for physiological imaging. Although the resolution of these techniques is only at the organ level, their high sensitivity endows them to be widely used in clinical medicine [16, 27-31]. These imaging techniques for mapping the metals and metalloids in living systems have recently been comprehensively reviewed elsewhere [4,
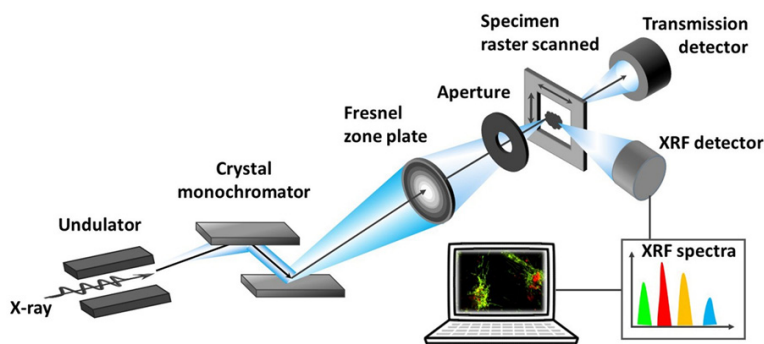
Figure 2. Schematic of an X-ray fluorescence microscope construction.

5, 23-26, 32, 33]. This review will particularly highlight the recent progresses of X-ray fluorescence imaging technology, a new and very promising one developed very recently.

X-Ray fluorescence imaging

XRF is an elemental analysis technique, which relies on recording the characteristic secondary X-rays emitted from specific atoms when the materials are irradiated by a focused X-ray beam [34]. The history of XRF dates back to 1895 when German physicist Wilhelm Conrad Röntgen accidentally discovered X-rays during his study of cathode rays in high-voltage, gaseous discharge tube. Based on Röntgen's discovery, Henry Moseley in 1913 discovered a mathematical relationship between the atom number (Z) and emitted X-ray wavelength. The technique was quickly realized to quantitative analysis of materials using XRF in 1914-1924. While the X-rays have been employed as a standard elemental analysis since 1950s when the first commercial XRF spectrometer was developed [35]. Since then, XRF has attracted increasing consideration and the relevant technique has been widely used for non-invasive imaging of thick and deep biological specimens with high spatial and temporal resolution [36].

As one of the advanced imaging approaches, X-ray fluorescence (XRF) imaging is a powerful technique for the quantitative mapping of distributions and dynamics of elements and chemical species at the spatial submicrometer resolution within biological samples [16, 18, 34, 37]. The physical principle of the XRF is illustrated in **Figure 1**. Upon excitation by an X-ray photon, a core-shell electron from the specific atom is ejected as a photoelectron. The formed core-hole is then filled by a neighbouring higher energy orbital electron, which results in emission of an X-ray fluorescence photon. The energy of the emitted photon is equal to the difference in binding energies of the two shells involved in the transition [27, 37]. Since the binding energy is varied with the nuclear charge, each element has a unique photon energy, *i.e.,* characteristic fingerprint X-ray fluorescence, which enables the multi-element analysis.

Apart from the conventional XRF microprobe, different variations of XRF imaging techniques, such as synchrotron X-ray fluorescence imaging (SXRFI) [16, 27, 34, 37], X-ray fluorescence computed tomography (XRFCT) [16, 27, 38], confocal XRF (CXRF) [39, 40], and total-reflection X-ray fluorescence imaging (TXRFI) [41] have been reported in recent years. Among these techniques, SXRFI has the highest element sensitivity due to absence of the bremsstrahlung background, while XRFCT can provide three-dimensional elemental composition in a sample [27, 34]. Therefore, these two techniques are most widely used for the imaging of metals in biological samples.

In particular, SXRFI is a microanalytical technique for mapping the spatial distribution of elements [18, 34, 42-45]. Due to the unique fluorescence spectrum of each element, simultaneous multi-element analysis can be achieved using SXRFI with qualitative and quantitative modalities. Compared with the conventional micro-XRF (m-XRF), synchrotron X-ray source-equipped SXRFI shows higher sensitivity with the detection limit estimated between 5.0×10^{-20} and 3.9×10^{-19} mol/mm^2 and the spatial resolution improved to 150 nm for the imaging of trace elements [18, 46, 47]. By virtue of deep penetration of synchrotron X-rays, this technique is highly applicable for mapping the metals in biological samples, such as in whole cells or tissue at single cell and subcellular resolution. A variety of cellular studies utilizing SXRF have been conducted, especially the investigation of distribution and abundance of metals in biological samples.

171
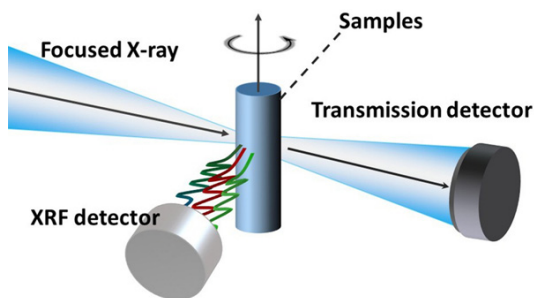
Figure 3. Schematic of a typical XRFCT rotation stage. The XRF is collected by a XRF detector, and X-ray attenuation is recorded by a transmission detector.

The apparatus of SXRFI typically consists of X-ray source, undulator, crystal monochromator, focusing optics, motorized sample stage, X-ray fluorescence, and transmission detector (**Figure 2**) [18, 27, 34, 38, 48]. Undulator is used to boast a smaller source size of X-ray and produce a beam with enhanced brightness. To select the band of the incident X-ray beam, a crystal monochromator is equipped. The selected X-ray is then focused on the specimen through a Fresnel zone plate [49]. An energy dispersive detector is applied to record the information of multi-element simultaneously. The orientation of biological samples on the specimen scanning stage is corrected by the help of transmission detector.

Due to its capability of 3-D elemental mapping within the sample, XRFCT has attracted increasing attention for imaging metals in biological samples in recently years [50, 51]. This technique integrates the CT imaging of X-ray attenuation with typical secondary XRF, and thus the 3-D elemental mapping can be obtained by stacking and combining 2-D XRF imaging. Using XRFCT, the specimen is irradiated by a micro- or nano-focused X-ray beam, and the secondary X-ray is collected with an X-ray dispersive detector to record the energy of each XRF photon [27, 34]. The XRF detector is designed to be 90° position to the incident X-ray beam to minimize the elastic and Compton scattered photons and improve the signal-to-background ratio [27, 52, 53]. The conventional XRFI apparatus (**Figure 2**) with an additional rotation stage is used as the microscope for the XRFCT [54].

The rotation of the XRFCT microscope is illustrated in **Figure 3**. For the sample with low elemental abundance, the scanning and rotation of the sample along a series of angles is

often used [50, 55, 56]. The focused X-ray beam is raster scanned through the sample, and the XRF intensity is recorded by the XRF detector at each orientation [27]. Typically, the measurement of a single slice of the sample requires several hours, which limits its application in live biological samples. Fortunately, thanks for the improvement of XRF detectors and fast detector electronics, "on-the-fly" sample scanning modality can reduce the X-ray irradiation time, and the live sample 3-D XRFCT is possible [55, 57]. In the case of high elemental abundance (*circa* > 1 wt%), full-field mode of XRFCT with a wide-fan X-ray beam can be used for the specific elemental mapping. With the wide-fan X-ray beam, only several minutes is required to map the metals in biological samples [34, 58]. Thus, a large dimension of the sample can be imaged using such a technique with low risk of radiation damage.

XRFCT is a non-invasive and highly sensitive technique for imaging metals with the 3-D model in living samples. In the XRFCT measurement, the pre-treatment of the biological samples, such as staining, fixation, and washing, is not required, which allows the accurate detection of metals in its native condition. The mapping of elemental abundance in living samples can be in the range of submicrogram per gram with a high spatial resolution (hundreds of nanometers) [59]. In addition, similar to the SXRFI, simultaneous multi-element analysis with qualitative and quantitative mode is also possible for XRFCT [27, 34].

Considering the essential roles of metals and metalloids in living systems and the unique advances of X-ray fluorescence imaging, we will highlight the recent progresses in this review on using XRF imaging technique to examine metals and metalloids in biological systems. We will focus on the application of XRF imaging in the investigation of toxicology and roles of metals and metalloids, in particular in various diseases at the organ and tissue level, and at cellular or even subcellular level. In addition, the current and future challenges in this field in terms of X-ray fluorescence development and applications are also discussed.

XRF imaging of toxic elements

It has been reported that some of the heavy metals and metalloids, especially Cr, Co, Pb,

Table 3. Typical toxicities of the most encountered metals and metalloids, and their treatment

Metal	Acute	Chronic	Toxic concentration	Treatment
As	Nausea, vomiting, "rice-water" diarrhea, encephalopathy, multi-organ dysfunction syndrome, long QT syndrome, painful neuropathy	Diabetes, hypopigmentation/ hyperkeratosis, cancer: lung, bladder, skin, encephalopathy	24 h urine: $\geq$50 µg/L urine, or 100 µg/g creatinine	BAL (acute, symptomatic) Succimer DMPS (Europe)
Cr	GI hemorrhage, hemolysis, acute renal failure (Cr^{6+} ingestion)	Pulmonary fibrosis, lung cancer (inhalation)	No clear reference standard	N-cetylcysteine (experimental)
Co	Beer drinker's (dilated) cardiomyopathy	Pneumoconiosis (inhaled); goiter	Normal excretion: 0.1-1.2 µg/L (serum) 0.1-2.2 µg/L (urine)	NAC $CaNa_2$ EDTA
Hg	Elemental (inhaled): fever, vomiting, diarrhea, acute lung injury; Inorganic salts (ingestion): caustic gastroenteritis	Nausea, metallic taste, gingivostomatitis, tremor, neurasthenia, nephrotic syndrome; hypersensitivity (Pink disease)	Background exposure "normal" limits: 10 µg/L (whole blood); 20 µg/L (24-h urine)	BAL Succimer 2,3-dimercapto-1-propane-sulfonic acid
Pb	Nausea, vomiting, encephalopathy (headache, seizures, ataxia, obtundation)	Encephalopathy, anemia, abdominal pain, nephropathy, foot-drop/wrist-drop	Pediatric: symptoms or [Pb] $\geq$45 µ/dL (blood); Adult: symptoms or [Pb] $\geq$70 µg/dL	BAL $CaNa_2$ EDTA Succimer
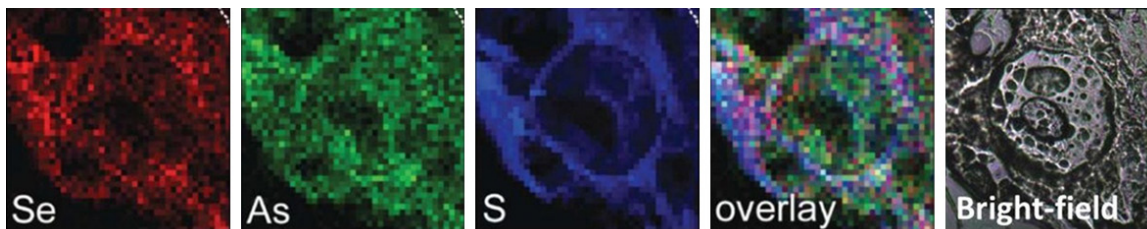
Figure 4. Micro-XRF element mapping of hyperplastic epidermis taken from the skin of a mouse exposed to ultraviolet radiation (UVR) and As (III) for 182 days. These images pointed out the differing subcellular distributions of As and Se in mice given As (III) only, particularly in the overlay, where As was clearly evident throughout the nucleus (excluding the nucleus), whereas Se was concentrated in the peripheral region of the cells. Scale bar 100 mm. Adapted from Environmental Health Perspectives, reference [68].

Hg, As, are highly toxic to human health and the environment. In biological systems, these elements have been reported to affect cellular organelles and components, such as cell membrane, mitochondrion, lysosome, endoplasmic reticulum, nuclei, and some enzymes involved in metabolism, detoxification, and repair of damages [60]. The relative toxicities, symptoms, and the corresponding treatment are listed in **Table 3** [61, 62]. It has been demonstrated that the mechanisms of toxicity and carcinogenicity of metals and metalloids are relevant to the reactive oxygen species (ROS) production and oxidative stress. Here, we will briefly summarize the progresses of XRF imaging for the most commonly encountered toxic metalloids and metals, including As, Cr, Co, Pb, and Hg in living systems.

As imaging

Arsenic (As) is widely distributed in the earth via both natural and anthropogenic pathways [63]. Despite its reputation as a deadly poison, As may be a necessary ultratrace element for some biological systems, such as red algae, chickens, rats, goats, and pigs. Excessive arsenic exposure has been associated with increased incidence of cancers, including lung cancers, skin cancers, and urinary bladder carcinoma in humans [64]. Compared to the reports on heavy metals, limited XRF imaging has been conducted to determine the quantitative spatial distribution of As in live cells and tissues, insects, and vertebrate samples such as fur and feathers.

XRF imaging has been applied to visualize the As distribution in HepG2 human hepatoma cells after exposure to arsenite (1 mM) or arsenate (20 mM). Munro et al. found that As was accumulated in the euchromatin region of the cell nucleus (following arsenite exposure), in accordance with As targeting DNA or proteins involved in DNA transcription [65]. The distribution, toxicity and biotransformation of arsenate in different life stages (larvae, pupae and adults) of a bertha armyworm moth (Mamestra configurata Walker) (Lepidoptera: Noctuidae) were investigated by Andrahennadi et al., and XRF imaging revealed the localized arsenic species, as well as zinc and copper within the gut [66].

Arsenic accumulation induced by chronic intake of arsenic-contaminated water has been examined in rat brain using the XRF imaging. The data showed that the accumulation of As was not linearly proportional to the treated arsenic dose, suggesting the existence of a protection mechanism that limits the transport of inorganic arsenic to the brain. The uniform spatial distribution of As was found, which is probably caused by the homogenous blood spreading to the brain [67]. The spatial distribution of As (and Se) has been evaluated at the cellular and subcellular levels in the skin of mice (**Figure 4**) [68]. Interestingly, the supplemental Se was found being effective preventing As accumulation in skin, suggesting the As-blocking effect of Se.

XRF imaging has also been applied to study the toxicity of As in vertebrate samples, such as fur and feathers. For example, using XRF elemental mapping of the hair, Kempson revealed that the cause-of-death of Phar Lap, a successful and famous racehorse, could be As poison [69].

Hg imaging

Hg is a unique heavy metal that exists in three types of chemical species: elemental Hg, inor-
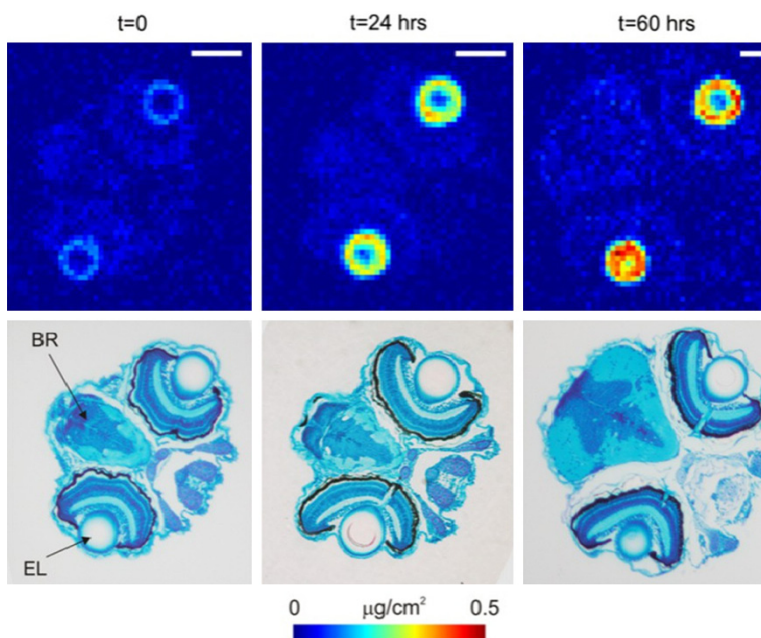
Figure 5. Histological images (lower) of head and XRF imaging (upper) quantitative Hg distributions in zebrafish larvae after a 12-h exposure to 2 µM methyl-Hg L-cysteineate (t = 0) followed by recovery time t = 24 h or 60 h in fresh system water. Scale bar 100 mm, BR: brain, EL: eye lens. Scale bar 100 mm. Adapted from JBIC Journal of Biological Inorganic Chemistry reference [73] with permission.

ganic Hg, and organic Hg [63]. The Hg compounds are well known as the most toxic species [70]. Despite their extreme toxicity, humans and animals are all unable to avoid exposure to some forms of Hg because some Hg compounds are ubiquitous in the environment. However, it remains difficult to investigate the Hg uptake mechanism and the interactions with biological species [71]. XRF has been recently reported to visualize the uptake and distribution of Hg in living systems, such as larval stage zebrafish, human brain tissue, teeth, and human bones.

Using synchrotron X-ray fluorescence mapping, Korbas et al. examined the uptake and localization of organic Hg in zebrafish larvae [72]. They found that methyl and ethyl Hg compounds were mainly accumulated in the rapidly dividing lens epithelium, with lower levels in the brain, optic nerve and various other organs, implying the direct effects of Hg on the ocular tissue. The detailed mechanism underlying organic Hg transport and accumulation has been then investigated [73]. As shown in **Figure 5**, redistribution of Hg to the eye lens was observed after removal of fish from treatment solutions (contaminated with methyl-Hg L-cysteineate), indicating that eye lens are the major sink for methyl-Hg in early embryonic and larval stages.

Inorganic Hg uptake and distribution were also investigated by Korbas et al. [74]. Unlike the methyl-Hg species [75], inorganic Hg was highly concentrated in olfactory epithelium and kidney in the absence of L-cysteine. However, with L-cysteine present in the treatment solution, mercuric bis-L-cysteineate species dominated the treatment, significantly decreasing uptake. In addition, quantitative XRF imaging was used to analyze Hg uptake in the absence and presence of 1-phenyl-2-thiourea (PTU), a widely used inhibitor to generate essentially transparent organisms for larval zebrafish [76]. The Hg concentration in the fish treated with solution of PTU + $HgCl_2$ was 60-fold lower than that in fish exposed to $HgCl_2$ solution. In contrast, both head and trunk sections of the larvae treated with CH_3HgCl and PTU had two fold higher Hg than in those treated with CH_3HgCl alone.

XRF imaging has also been employed to study the co-localization of Hg in biological samples [77]. When the human brain tissues were poisoned by methyl-Hg, Hg and Se were co-localized in the grey matter in the form of HgSe nanoparticle [78]. Exposure of larval zebrafish to inorganic Hg also showed nano-scale structures containing co-localized Hg and Se [79]. Supported by the microscaled X-ray absorption analysis, the co-localized deposits were most likely comprised of highly insoluble mixed chalcogenide $HgS_xSe_{(1-x)}$ where x was 0.4-0.9, probably with the cubic zincblende structure.

Spatial distribution of Hg in human teeth filled with amalgams for more than 20 years has been determined by XRF imaging analysis [80]. Up to ~10 mg/g Hg was detected in the dentinal tubules several millimetres away from the
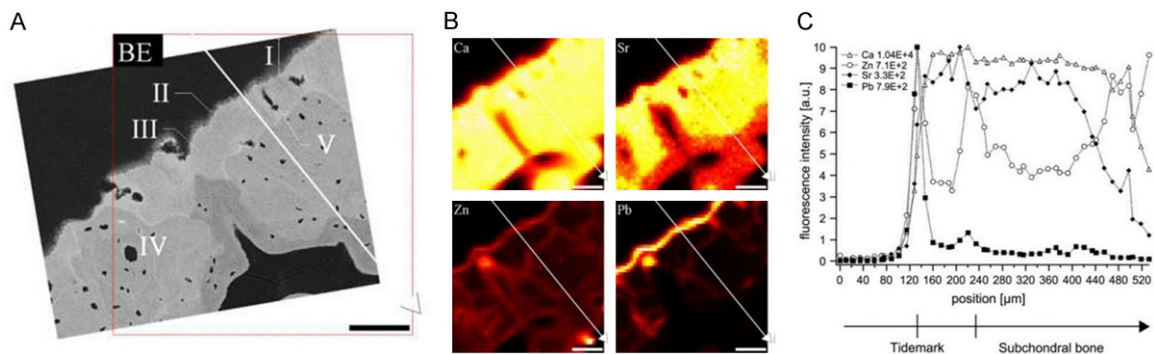
Figure 6. A. Backscattered electron (BE) image of analyzed chondral/subchondral region of the patella. Non-calcified cartilage (I), tidemark (II), calcified cartilage (III), subchondral bone (IV), and cement-lines (V) can be clearly identified. Length of scale bar: 100 mm. B. Ca, Zn, Sr, Pb signal intensity mapping in the corresponding region. C. Fluorescence intensity profiles along the marked line. Maximum fluorescence intensities were normalized to 10. Pb and Zn maxima can be exactly allocated to the tidemark of articular cartilage. Scale bar 100 mm. Adapted from Osteoarthritis and Cartilage reference [83] with permission.

amalgam location. In addition to Hg in human teeth, XRF imaging has been also employed to determine whether Hg is present in the bone as a result of environmental contamination or due to biogenic uptake [81]. The results revealed that Hg existed in part of the localized subset of the osteons.

Pb imaging

Pb is a toxic heavy metal that is taken up by the human body through food, drinking water, and inhalation, and is excreted via the gastrointestinal tract and the renal system [63]. Exposure to Pb is associated with chronic diseases in the nervous, hematopoietic, skeletal, renal and endocrine systems. It is known that Pb accumulates in the skeleton [82]. Thus, the understanding of Pb toxicity is of great importance due to the lack of treatment options for Pb-induced diseases.

XRF imaging could make a significant contribution, although to date only a few XRF imaging studies have been reported about Pb in animal systems. In 2006, Zoeger et al. used high resolution XRF imaging to determine the spatial distribution of Pb and other trace elements in normal articular cartilage and subchondral bone from adult humans with no history of work-related exposure to Pb [83]. As shown in **Figure 6**, a highly specific accumulation of Pb occurred in the tidemark, the transition zone between calcified and non-calcified articular cartilage. Quantitative fluorescence analysis revealed that a 13-fold higher Pb concentra-

tion was in the tidemark of articular cartilage when compared to subchondral bone [83]. The observation was further confirmed by the same research team through investigation of the osteochondral samples, which were long-term treated to increased lead (Pb) concentrations [84, 85].

The distribution of Pb in the human bone tissue has been also determined by XRF imaging [86-88]. The studies conducted by Zoeger et al. revealed that Pb was mostly located at the outer border of the cortical bone in various samples [87]. A remarkable association between Pb and Zn content can also be observed. Pemmer et al. reported that the levels of Pb and Zn were significantly higher in the cement lines than the adjacent mineralized bone matrix, possibly due to the different uptake mechanism [86]. Arora et al. reported the first application of XRF imaging technique in measuring the distribution of Zn and Pb in the ameloblasts in developing Wistar rat teeth. Results showed that Pb was only visualized reliably in developing enamel but not in ameloblasts [89]. Interestingly, XRF imaging has been reported as a useful technology in archaeological studies, and used to analyze bone and hair samples from Ferrante II of Aragon, King of Naples (1469-1496) and Isabella of Aragon, Duchess of Milan (1470-1524). Results showed that Pb was localized to microanatomical locations, consistent with bone remodelling events and compositionally similar to Pb-substituted hydroxyapatite, i.e. Pb binding in bone [90].
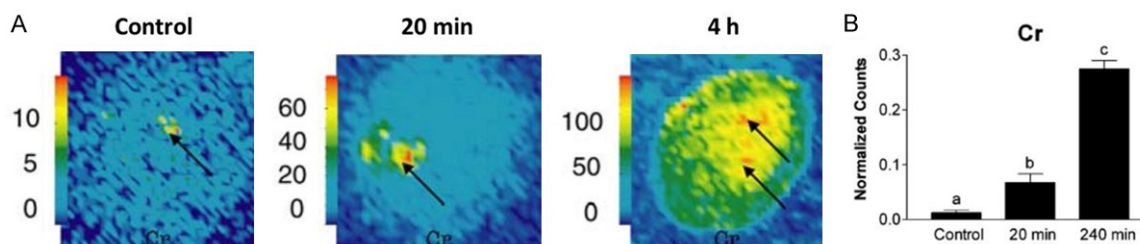
Figure 7. Distribution mapping (A) and relative amount (B) taken up by single A549 human lung carcinoma cell treated with 100 μM Cr(VI) in comparison with untreated cells. Adapted from JBIC Journal of Biological Inorganic Chemistry reference [99] with permission.

Co imaging

Co is very much widespread in the natural environment [91]. For humans, Co is an essential trace element required for the generation of vitamin B_{12}. However, it becomes toxic at high concentrations, thus leading to adverse health effects [16]. There are a few studies done to investigate Co toxicity, uptake, transport, and distribution using XRF imaging analysis [92, 93].

In 2009, XRF imaging analysis in tomography mode was performed for the first time on a single cell (HaCaT human keratinocytes) to determine the 3D intracellular distribution of cobalt [93]. The images showed that Co was distributed in the nucleus and perinuclear region in HaCaT cells, implying the possible direct interactions with genomic DNA and nuclear proteins. The perinuclear accumulation in the cytosol suggests that cobalt could be stored in the endoplasmic reticulum or the Golgi apparatus. In addition, when the cells were exposed to exogenous Co, a decreasing level of Zn and Mg was found, indicating a likely replacement Mg and Zn by Co in protein binding sites.

Cr imaging

Cr plays important roles in biological functions of life, but can become toxic at higher doses. Its toxicity is also dependent on its chemical state [63]. It is well known that Cr compounds are stable in both trivalent [Cr(III)] and hexavalent [Cr(VI)] state. Exposure of human beings and animals to Cr has been a major concern because of the high risk of Cr-induced cancers, such as lung cancer [94]. A generally accepted mechanism for Cr(VI)-induced genotoxicity and cancers includes intracellular internalization (through anion channels for water-soluble chromates or phagocytosis of insoluble chromates),

transport, reduction to Cr(III), and then formation of Cr-DNA and Cr-protein complexes.

The mechanism of Cr toxicity in live systems can be directly examined by XRF imaging [95]. The investigation conducted by Fayard et al. showed homogenous distribution of Cr in Chinese Hamster Ovary cells (CHO-AA8) exposed *in vitro* to both soluble and insoluble Cr compounds. Interestingly, Cr(VI) was not detected, suggesting a mechanism of rapid intracellular reduction [96]. Further studies in the same group confirmed the reduction of Cr(VI) to Cr(III) and revealed the distribution in nucleus of Institut Gustave Roussy ovarian cell line 1 (IGR-OV1) cells [97]. Cr seemed to accumulate P-rich regions, such as nucleus and the area outside the nucleus (acidic vacuole), as reported by Dillon et al. in V79 Chinese hamster lung cells. This accumulation may indicate that Cr is capable of targeting the DNA and causing the genotoxic damage [98].

Using XRF imaging, Harris et al. investigated the dynamic process of intracellular uptake, distribution, and biotransformation of Cr(VI) in human lung cells [99]. A549 human lung adenocarcinoma epithelial cells were treated with Cr(VI) at 100 mM for 20 min and 4 h, respectively. As shown in **Figure 7**, Cr was found in a small area of cytoplasm after 20 min treatment, while distributed to whole cells after 4 h treatment due to uptake of more Cr. Interestingly, a higher Cr concentration in the nucleus and cytoplasmic membrane was still observed, indicating the accumulation in the nucleus and the cytosol [97].

XRF imaging of metals for various diseases

Imaging of metals in cancer research

The association of metal exposure with cancers is well documented [100]. Currently, met-

als are thought to promote cancer development by a number of mechanisms, such as inducing reactive oxygen species (ROS) to oxidatively damage DNA, protein, and lipids [101, 102]. Thus, XRF imaging technique has been actively used to study the relationship between the metal concentrations and a number of cancers, including breast cancer, prostate cancer, and colorectal cancer recently [56, 103-105].

XRF has been applied to image K, Fe, Cu, Zn, and Ca in breast cancer [106-108]. Compared to that in the normal tissues, the concentration of assessed metals increased in the tumour region, especially Zn and Cu [106, 109, 110]. Further investigation by Farquharson et al. confirmed the increasing concentration of Ca, Cu, and Zn in the tumour lesion, but a lower concentration of Fe in some of the tested samples [109, 111]. Zn is being considered as a possible marker of human prostate cancer [112]. Using XRF imaging, Ide-Ektessabi reported that the Zn concentration is significantly lower in prostate cancer tissues compared with that in health specimens [113]. This finding was further confirmed by Podgórczyk et al. [112]. The correlation between Zn and Ca suggested that Ca mediated Zn accumulation in prostate cancer tissues [114].

Metals in other cancer lesions and organs have been also investigated using XRF imaging technology. The localization and the relative concentration of Zn, Cu, Fe and Ca in primary colorectal cancer and secondary colorectal liver metastases were examined by Al-Ebraheem et al. Significant increase in the concentration of Zn, Ca, Cu and Fe was found in necrotic tissues [115]. They also quantified the concentration of Fe, Cu, Zn, and K in normal and malignant liver and kidney tissues. The data indicated that the Zn concentration was reduced by 63% and 26% in liver and kidney tumors, respectively. Fe, Cu, and K concentrations were increased in kidney tumors by 150%, 8% and 90%, but reduced in liver tumors by 76%, 29% and 43%, respectively [116].

Among all metals investigated in cancer research, Cu is special due to its special roles in cancer development [111]. It is well known that angiogenesis is vital for supplying oxygen for the tumor growth. Thus, depletion of Cu has been shown to inhibit angiogenesis in a wide variety of cancer cells and xenograft systems

[117]. Using XRF imaging, Finney et al. investigated the localization and roles of Cu in angiogenesis system. They found that Cu was remarkably redistributed from intracellular compartments to the tips of nascent endothelial cell filopodia and across the cell membrane [118].

Imaging of metals for neurodegenerative diseases

The brain is rich in metals, such as Fe, Cu, and Zn as essential cofactors in metalloproteins, and Hg and Pb as neurotoxins [119, 120]. These metals have been implicated in various neurodegenerative diseases, including Alzheimer's disease, Parkinson's disease, amyotrophic lateral sclerosis (ALS), prion diseases, and Huntington's disease [121]. There is increasing investigation of precise roles of these metals in neurodegenerative diseases using XRF imaging technology [122].

Utilizing XRF imaging, Pushie et al. investigated the level and distribution of Cu, Fe and Zn in the brain of mice that express different levels of prion protein (PrP^c), a family of fatal neurodegenerate diseases [123]. Results suggested that the amount and distribution of specific metals within the central nervous system is regulated by the PrP^c. Subcellular distribution of metals in a childhood neurodegenerative disorder revealed that Zn nuclear-to-cytoplasmic trafficking was perturbed in diseased cells and the Ca subcellular distribution was drastically altered in Cb*Cln6*^{nclf} cells [124].

Mn is well known as the magnetic resonance imaging (MRI) reagent in vivo. However, it is reported that Mn is neurotoxic, by accumulating in the hippocampal formation (HPCf) of brain and causing symptoms similar to those associated with Parkinson's disease [125, 126]. Thus, Robison et al. examined the distribution of Mn in the HPCf for Sprague-Dawley rats with chronic Mn exposure, and quantitatively compared Mn distribution with that of other biologically relevant metals, such as Fe, Cu and Zn [127]. In consistence with MRI results, an increasing Mn concentration in hippocampal, especially in the dentate gyrus (DG) and the cornus ammonis 3 (CA3) layer, was observed. In addition, significant spatial correlation of Mn-Zn was observed across the HPCf substructures (**Figure 8**).
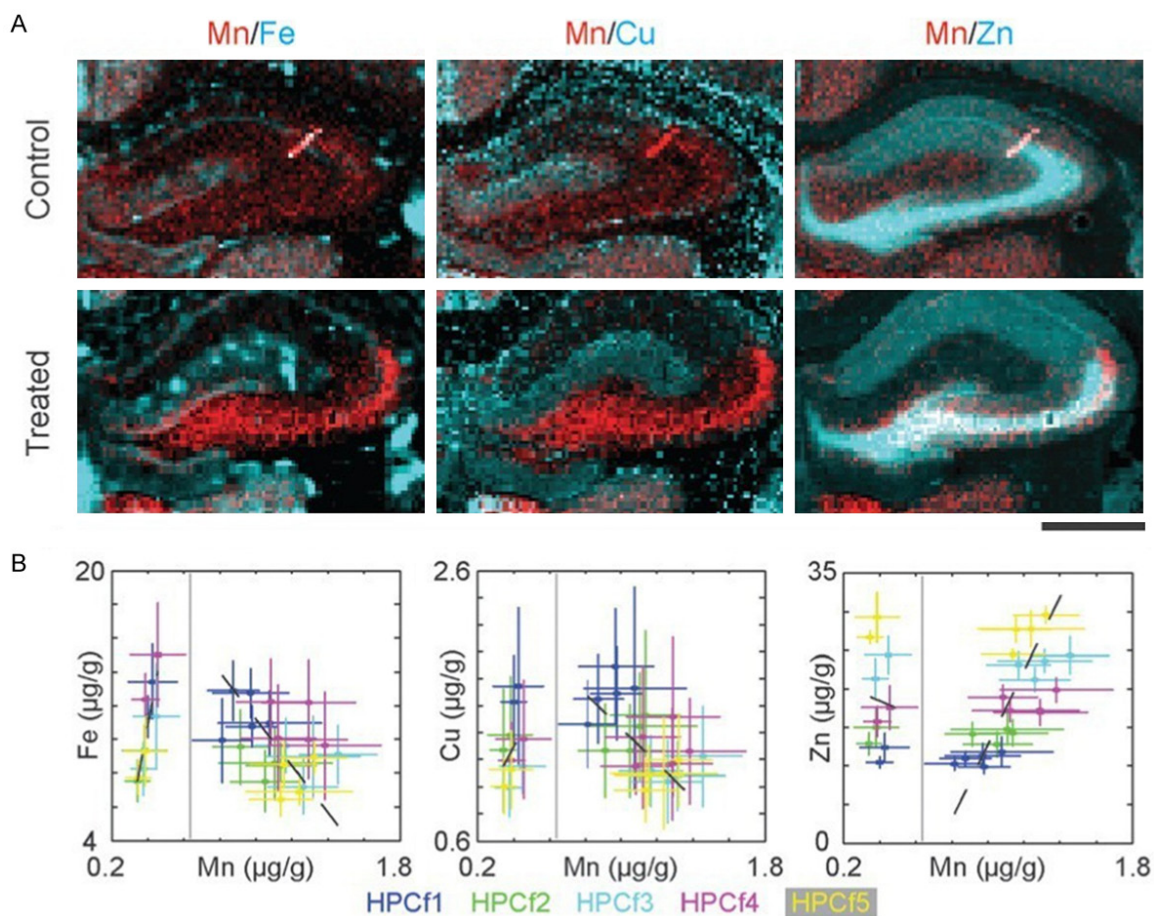
Figure 8. Analysis of the hippocampal formation regions. A. Two colored images displaying Fe-Mn, Cu-Mn, and Zn-Mn respectively. Note that Mn and Zn co-localized in the CA3 of the HPCf, while a small portion of Mn also co-localized with Fe within the DG as indicated by white pixels in the images. Scale bar: 1 mm. B. Scatter plots of the mean metal concentrations in regions identified by clustering. Scale bar 1 mm. Reproduced from reference [127] with permission of The Royal Society of Chemistry.

XRF imaging was also used to investigate the roles of metals associated with stroke [128] and epilepsy [129-132]. Images showed that Cu plays important roles in the pathogenesis of epilepsy in the Wistar rats. Lower levels of Cu were found in the latent period compared with the control group and even in the acute period [131]. In quantitative analysis of rat brain undergoing pilocarpine-induced epilepsy, a relatively lower Cu level was found in the dentate gyrus, and a lower Zn level in the hippocampus and dentate gyrus, where a higher Ca level was observed in this area [132].

Alzheimer's disease (AD) is the leading cause of dementia in the elderly, affecting more than 27 million people worldwide (about 2% population in the developed world [133-135]. It is one of the most prevalent and debilitating

neurodegenerative diseases and yet it is typically diagnosed only after cognitive symptoms appear, which is normally too late for effective treatment [134]. Pathologically, AD is characterized by extracellular amyloid plaques composed of insoluble amyloid beta (Aβ) protein, and intra-neuronal neurofibrillary tangles (NF-Ts) containing hyperphosphorylated tau protein. At the molecular level, metals, including Cu, Zn and Fe, have been confirmed as neurochemical factors to be involved in the metabolism and functional expression of Aβ and amyloid precursor protein (APP) [135].

XRF imaging has been developed for the quantitative analysis of metal metabolism in animal models (**Figure 9**) [136]. The observations reported by Leskovjan et al. revealed that the level of Zn, Cu, Ca, and Fe was all increased in
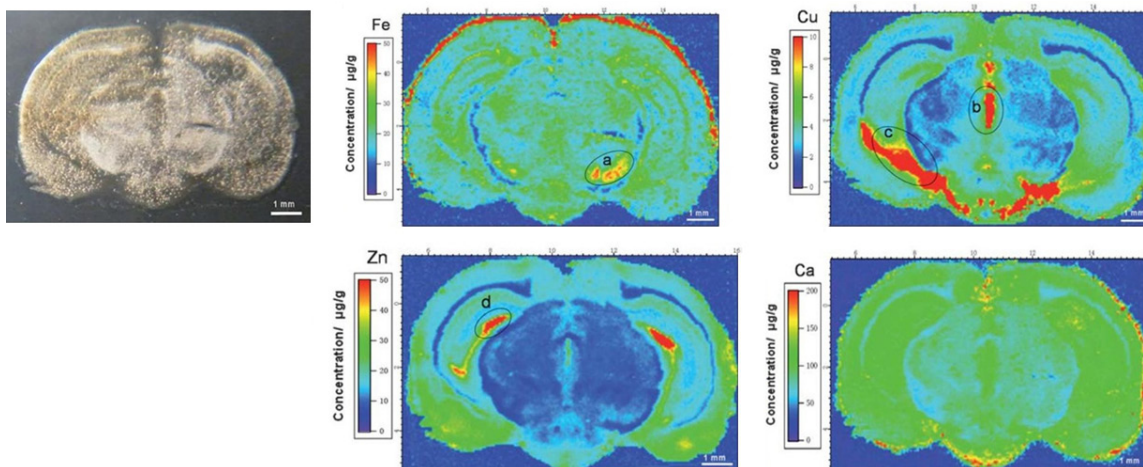
Figure 9. The quantitative images of Ca, Fe, Cu and Zn in the brain section of Alzheimer's disease mouse. a: Substantia nigra region, b: Superior colliculus, c: CA3 area of hippocampus, d: Dentate gyrus region. Scale bar 1 mm. Adapted from reference [136] with permission of The Royal Society of Chemistry.

human amyloid plaques, suggesting that these metals are involved in neurodegeneration [137]. Further studies on the time course of the metal concentration and distribution by the same group revealed that Fe in the cortex was 34% higher than age-matched controls at an early stage, corresponding to the commencement of plaque formation [138]. Using XRF imaging, Wang et al. found that Fe and Ca level increased with brain aging in both AD and control mice, while the level of Cu, Fe, Zn and Ca appeared significantly high in AD mice and showed an obvious age-dependent rise [139]. The increase of Zn in a small regional hippocampal was also confirmed by Adlard et al. *via* XRF imaging [140].

Parkinson's disease (PD) is a progressive neurological condition [141]. PD is the most common serious movement disorder in the world, and affects about 1% adults older than 60 years and 4% populations older than 80 years. The most characteristic hallmark of PD is confirmed to be the loss of dopaminergic (DA) neurons within the substantia nigra pars compacta (SNc). Nevertheless, the triggers for these events are still unclear [142, 143], while the changes in biometals in brain have long been suspected to play a key role in the PD development. Recently, XRF imaging has been evaluated by mapping and quantifying metals, such as Fe, Zn ad Cu in brain slices from PD and unaffected brains [144, 145].

Employing XRF imaging of trace elements in the pathogenesis of PD, Chwiej et al. demonstrated that elements P, Cl, Fe, Cu and Zn played important roles in the process of differentiation between neurons [145]. Due to the importance of Cu, Davies et al. investigated the changes in Cu and Cu-associated pathways in the vulnerable substantia nigra (SN) and locus coeruleus (LC) and non-degenerative brain regions. They found a significant decreasing in levels of Cu and Cu-transporter protein 1 in surviving neurons in the SN and LC in PD patients [146].

Robison et al. introduced XRF imaging as a new quantitative tool to determine the Mn distribution in the brain [147]. As shown in **Figure 10**, the highest Mn level was observed in the globus pallidus (GP), the thalamus (Th), and the substantia nigra pars compacta (SNc) in the brain. But following studies showed that Mn accumulation in SNc is higher than GP and Th. [126]. Ďučić et al. showed that Mn was localized in cytoplasmic/paranuclear in dopaminergic neurons after treated with Mn [148], while Mn was accumulated within Golgi apparatus in dopaminergic cells, PC-12 [149].

Conclusions and future perspectives

Over the past decade, XRF imaging technique for determining the level and distribution of metals and metalloids has been rapidly developed. This method has been recognized as an ideal tool to reliably determine the elemental distribution in tissue specimens at the cellular, even subcellular level with high sensitivity and low background. In this review, we have pre-
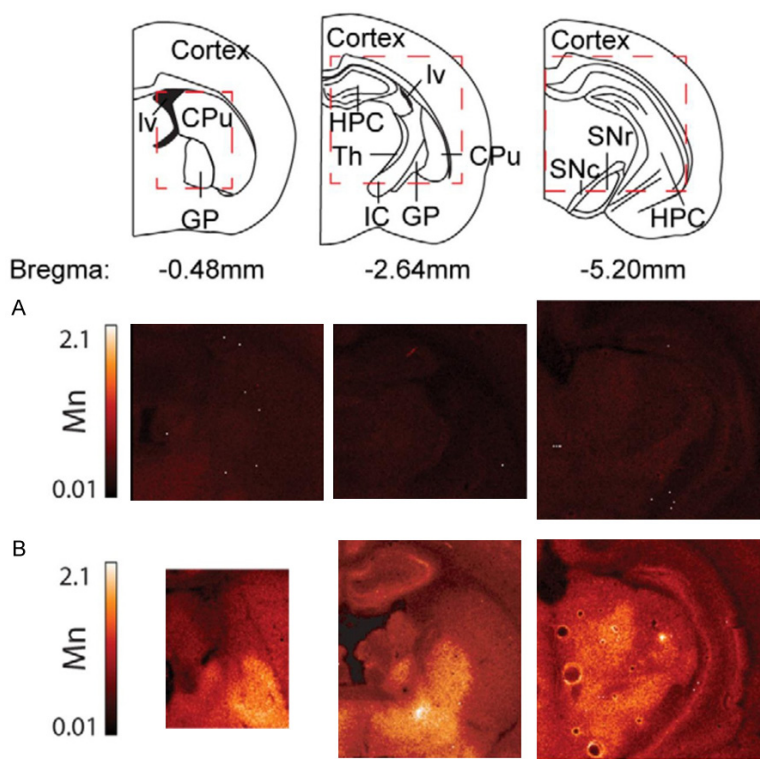
Figure 10. XRF imaging of Mn distribution in brain sections of control and treated rats. Mn distribution of coronal sections from untreated (control) rats (A) and Mn treated rats (B). AB, axonal bundle; CPu, caudate putamen; GP, globus pallidus; HPC, hippocampal formation; IC, internal capsule; lv, lateral ventricle; Th, thalamus; SNc, substantia nigra compacta; SNr, substantia nigra reticular. Scale bar 2 mm. Adapted from PLOS ONE, reference [147].

as well as metal metabolism, which may help reveal the detail mechanisms that metals or metalloids are involved in disease development. Thus, faster and more efficient imaging system with higher resolution will be an important research direction. The third challenge is the imaging sensitivity limitation. As summarized in this review, current applications of XRF imaging are mainly focused on the toxicology of metals and metalloids, and their possible physiopathology in cancers and neurodegenerative diseases. As a powerful imaging technology, XRF should be widely used to map the trace amount of elements in other diseases, such as cardiovascular diseases [150, 151], atheroscelerosis [152], and dental diseases [153, 154], improving our understanding of the roles that metals and metalloids play in the development of these diseases.

sented the general principle of XRF imaging and summarized the recent applications in determining the spatial distribution of metals and metalloids in biological specimens to examine their toxicology and their possible roles in development of various diseases. After a thorough survey of published papers, we are sure that XRF imaging will become a superior tool to study metals and metalloids in animals and humans in the near future.

However, this new technique has faced a few challenges in the future applications in life science. The first challenge is the imaging scan speed bottleneck. At current, the scan speed is relatively slow, so XRF imaging is still not suitable for high-throughput analysis. The second challenge is the limited imaging resolution. It is true that imaging of metals and metalloids has been reported at the cellular or even subcellular levels, higher resolution is still required to determine the distribution and understand the biomolecule-metal interactions

Acknowledgements

Disclosure of conflict of interest

None.

Address correspondence to: Zhi Ping Xu, Australian Institute for Bioengineering and Nanotechnology, The University of Queensland, Corner College and Cooper Rds, Brisbane QLD 4072, Australia. E-mail: gordonxu@uq.edu.au

References

[1] Domaille DW, Que EL and Chang CJ. Synthetic fluorescent sensors for studying the cell biology of metals. Nat Chem Biol 2008; 4: 168-175.
[2] Metals in chemical biology. Nat Chem Biol 2008; 4: 143-143.

[3]   Zecca L, Youdim MBH, Riederer P, Connor JR and Crichton RR. Iron, brain ageing and neurodegenerative disorders. Nat Rev Neurosci 2004; 5: 863-873.

[4]   Qian X and Xu Z. Fluorescence imaging of metal ions implicated in diseases. Chem Soc Rev 2015; 44: 4487-4493.

[5]   Susnea I and Weiskirchen R. Trace metal imaging in diagnostic of hepatic metal disease. Mass Spectrom Rev 2016; 35: 666-686.

[6]   Wasowicz W, Gromadzinska J, Rydzynski K and Tomczak J. Selenium status of low-selenium area residents: polish experience. Toxicol Lett 2003; 137: 95-101.

[7]   Andrews NC. Metal transporters and disease. Cur Opin Chem Biol 2002; 6: 181-186.

[8]   Sigel A and Sigel H. Metal ions in biological systems, volume 35: iron transport and storage microorganisms, plants, and animals. Metal-Based Drugs 1998; 5: 262.

[9]   Laurie SH. Transport and storage of metals. J Inherit Metab Dis 1983; 6: 9-14.

[10]   Williams RJ. Role of transition metal ions in biological processes. Royal Inst Chem Rev 1968; 1: 13-38.

[11]   Uauy R, Maass A and Araya M. Estimating risk from copper excess in human populations. Am J Clin Nutr 2008; 88: 867S-871S.

[12]   Meng Q, Shi Y, Wang C, Jia H, Gao X, Zhang R, Wang Y and Zhang Z. NBD-based fluorescent chemosensor for the selective quantification of copper and sulfide in an aqueous solution and living cells. Org Biomol Chem 2015; 13: 2918-2926.

[13]   Maity D, Manna AK, Karthigeyan D, Kundu TK, Pati SK and Govindaraju T. Visible-near-infrared and fluorescent copper sensors based on julolidine conjugates: selective detection and fluorescence imaging in living cells. Chem Eur J 2011; 17: 11152-11161.

[14]   Zhang R, Yu X, Yin Y, Ye Z, Wang G and Yuan J. Development of a heterobimetallic Ru(II)-Cu(II) complex for highly selective and sensitive luminescence sensing of sulfide anions. Anal Chim Acta 2011; 691: 83-88.

[15]   Maity D and Govindaraju T. Highly selective visible and near-IR sensing of Cu2+ based on thiourea-salicylaldehyde coordination in aqueous media. Chem Eur J 2011; 17: 1410-1414.

[16]   McRae R, Bagchi P, Sumalekshmy S and Fahrni CJ. In situ imaging of metals in cells and tissues. Chem Rev 2009; 109: 4780-4827.

[17]   Meng Q, Zhang R, Jia H, Gao X, Wang C, Shi Y, Everest-Dass AV and Zhang Z. A reversible fluorescence chemosensor for sequentially quantitative monitoring copper and sulfide in living cells. Talanta 2015; 143: 294-301.

[18]   Qin Z, Caruso JA, Lai B, Matusch A and Becker JS. Trace metal imaging with high spatial resolution: applications in biomedicine. Metallomics 2011; 3: 28-37.

[19]   Huang X, Lee S and Chen X. Design of "smart" probes for optical imaging of apoptosis. Am J Nucl Med Mol Imaging 2011; 1: 3-17.

[20]   Carter KP, Young AM and Palmer AE. Fluorescent sensors for measuring metal ions in living systems. Chem Rev 2014; 114: 4564-4601.

[21]   Dean KM, Qin Y and Palmer AE. Visualizing metal ions in cells: an overview of analytical techniques, approaches, and probes. BBA-Mol Cell Res 2012; 1823: 1406-1415.

[22]   Aragay G, Pons J and Merkoçi A. Recent trends in Macro-, Micro-, and nanomaterial-based tools and strategies for heavy-metal detection. Chem Rev 2011; 111: 3433-3458.

[23]   Becker JS, Matusch A, Becker JS, Wu B, Palm C, Becker AJ and Salber D. Mass spectrometric imaging (MSI) of metals using advanced brain-met techniques for biomedical research. Int J Mass Spectrom 2011; 307: 3-15.

[24]   Schwartz S and Caprioli R. Imaging mass spectrometry: viewing the future. In: Rubakhin SS, Sweedler JV, editors. Mass spectrometry imaging. Humana Press; 2010. pp. 3-19.

[25]   Yeung MC and Yam VW. Luminescent cation sensors: from host-guest chemistry, supramolecular chemistry to reaction-based mechanisms. Chem Soc Rev 2015; 44: 4192-4202.

[26]   Pal S, Chatterjee N and Bharadwaj PK. Selectively sensing first-row transition metal ions through fluorescence enhancement. RSC Adv 2014; 4: 26585-26620.

[27]   Chen H, Rogalski MM and Anker JN. Advances in functional X-ray imaging techniques and contrast agents. Phys Chem Chem Phys 2012; 14: 13469-13486.

[28]   Beekman FJ, van der Have F, Vastenhouw B, van der Linden AJA, van Rijk PP, Burbach JPH and Smidt MP. U-SPECT-I: a novel system for submillimeter-resolution tomography with radiolabeled molecules in mice. J Nucl Med 2005; 46: 1194-1200.

[29]   Rahmim A and Zaidi H. PET versus SPECT: strengths, limitations and challenges. Nucl Med Commun 2008; 29: 193-207.

[30]   Wang Y, Song R, Guo K, Meng Q, Zhang R, Kong X and Zhang Z. A gadolinium(iii) complex based dual-modal probe for MRI and fluorescence sensing of fluoride ions in aqueous medium and in vivo. Dalton Trans 2016; 45: 17616-17623.

[31]   Cheon J and Lee JH. Synergistically integrated nanoparticles as multimodal probes for nanobiotechnology. Acc Chem Res 2008; 41: 1630-1640.

[32]   Kaur K, Saini R, Kumar A, Luxami V, Kaur N, Singh P and Kumar S. Chemodosimeters: an approach for detection and estimation of bio-

logically and medically relevant metal ions, anions and thiols. Coord Chem Rev 2012; 256: 1992-2028.

[33] Formica M, Fusi V, Giorgi L and Micheloni M. New fluorescent chemosensors for metal ions in solution. Coordination Chem Rev 2012; 256: 170-192.

[34] Pushie MJ, Pickering IJ, Korbas M, Hackett MJ and George GN. Elemental and chemically specific X-ray fluorescence imaging of biological systems. Chem Rev 2014; 114: 8499-8541.

[35] Taylor M, Bytheway R, Tanner BK, Watanabe M, Isoyama G and Spielmann C. X-Ray sources. In: editors. X-Ray spectrometry: recent technological advances. John Wiley & Sons, Ltd; 2004. pp. 13-62.

[36] West M, Ellis AT, Potts PJ, Streli C, Vanhoof C, Wegrzynek D and Wobrauschek P. Atomic spectrometry update-X-ray fluorescence spectrometry. J Anal At Spectrom 2011; 26: 1919-1963.

[37] Fahrni CJ. Biological applications of X-ray fluorescence microscopy: exploring the subcellular topography and speciation of transition metals. Cur Opin Chem Biol 2007; 11: 121-127.

[38] Deng B, Yang Q, Du G, Tong Y, Xie H and Xiao T. The progress of X-ray fluorescence computed tomography at SSRF. Nucl Instrum Meth B 2013; 305: 5-8.

[39] Nakano K and Tsuji K. Development of laboratory confocal 3D-XRF spectrometer and nondestructive depth profiling. J Anal At Spectrom 2010; 25: 562-569.

[40] Dehlinger M, Fauquet C, Lavandier S, Aumporn O, Jandard F, Arkadiev V, Bjeoumikhov A and Tonneau D. Spatial resolution of confocal XRF technique using capillary optics. Nanoscale Res Lett 2013; 8: 271.

[41] Sakurai K. Total-reflection X-ray fluorescence imaging. Spectrochim Acta B 1999; 54: 1497-1503.

[42] Geil EC, LeBlanc SA, Dale DS and Thorne RE. Application of X-ray fluorescence imaging to ceramics from the American Southwest. J Archaeolog Sci 2013; 40: 4780-4784.

[43] Ortega R, Devès G and Carmona A. Bio-metals imaging and speciation in cells using proton and synchrotron radiation X-ray microspectroscopy. J R Soc Interface 2009; 15: S649-658

[44] Ortega R, Cloetens P, Devès G, Carmona A and Bohic S. Iron storage within dopamine neurovesicles revealed by chemical nano-imaging. PLoS One 2007; 2: e925.

[45] Vine DJ, Pelliccia D, Holzner C, Baines SB, Berry A, McNulty I, Vogt S, Peele AG and Nugent KA. Simultaneous X-ray fluorescence and ptychographic microscopy of cyclotella meneghiniana. Opt Exp 2012; 20: 18287-18296.

[46] Cotte M, Welcomme E, Solé VA, Salomé M, Menu M, Walter P and Susini J. Synchrotron-based X-ray spectromicroscopy used for the study of an atypical micrometric pigment in 16th century paintings. Anal Chem 2007; 79: 6988-6994.

[47] Somogyi A, Drakopoulos M, Vincze L, Vekemans B, Camerani C, Janssens K, Snigirev A and Adams F. ID18F: a new micro-x-ray fluorescence end-station at the European Synchrotron Radiation Facility (ESRF): preliminary results. X-Ray Spectrom 2001; 30: 242-252.

[48] Qiu J, Deng B, Yang Q, Yan F, Li A and Yu X. Internal elemental imaging by scanning X-ray fluorescence microtomography at the hard X-ray microprobe beamline of the SSRF: preliminary experimental results. Nucl Instrum Meth B 2011; 269: 2662-2666.

[49] Di Fabrizio E, Romanato F, Gentili M, Cabrini S, Kaulich B, Susini J and Barrett R. High-efficiency multilevel zone plates for keV X-rays. Nature 1999; 401: 895-898.

[50] Lombi E, de Jonge MD, Donner E, Ryan CG and Paterson D. Trends in hard X-ray fluorescence mapping: environmental applications in the age of fast detectors. Anal Bioanal Chem 2011; 400: 1637-1644.

[51] Kim SA, Punshon T, Lanzirotti A, Li L, Alonso JM, Ecker JR, Kaplan J and Guerinot ML. Localization of iron in arabidopsis seed requires the vacuolar membrane transporter VIT1. Science 2006; 314: 1295-1298.

[52] Patrick JL. Approximate analytic reconstruction in x-ray fluorescence computed tomography. Phys Med Biol 2004; 49: 2391-405.

[53] Eduardo XM and Alvaro RDP. Exact analytic reconstruction in x-ray fluorescence CT and approximated versions. Phys Med Biol 2010; 55: 1007-24.

[54] Bleuet P, Welcomme E, Dooryhee E, Susini J, Hodeau JL and Walter P. Probing the structure of heterogeneous diluted materials by diffraction tomography. Nat Mater 2008; 7: 468-472.

[55] Sarret G, Smits EAHP, Michel HC, Isaure MP, Zhao FJ and Tappero R. Chapter one-use of synchrotron-based techniques to elucidate metal uptake and metabolism in plants. In: Donald LS, editor. Adv Agron. Academic Press; 2013. pp. 1-82.

[56] Pereira GR, Anjos MJ, Rocha HS, Faria P, Pérez CA and Lopes RT. Computed tomography and X-ray fluorescence CT of biological samples. Nucl Instrum Meth A 2007; 580: 951-954.

[57] de Jonge MD and Vogt S. Hard X-ray fluorescence tomography-an emerging tool for structural visualization. Cur Opin Struct Biol 2010; 20: 606-614.

[58] Sutton SR, Bertsch PM, Newville M, Rivers M, Lanzirotti A and Eng P. Microfluorescence and

microtomography analyses of heterogeneous earth and environmental materials. Rev Mineral Geochem 2002; 49: 429-483.

[59] de Jonge MD, Holzner C, Baines SB, Twining BS, Ignatyev K, Diaz J, Howard DL, Legnini D, Miceli A, McNulty I, Jacobsen CJ and Vogt S. Quantitative 3D elemental microtomography of cyclotella meneghiniana at 400-nm resolution. Proc Natl Acad Sci U S A 2010; 107: 15676-15680.

[60] Bower JJ, Leonard SS and Shi X. Conference overview: molecular mechanisms of metal toxicity and carcinogenesis. Mol Cell Biochem 2005; 279: 3-15.

[61] Flora S. Metal poisoning: threat and management. Al Ameen J Med Sci 2009; 2: 4-26.

[62] Rafati-Rahimzadeh M, Rafati-Rahimzadeh M, Kazemi S and Moghadamnia A. Current approaches of the management of mercury poisoning: need of the hour. DARU 2014; 22: 46.

[63] Tchounwou PB, Yedjou CG, Patlolla AK and Sutton DJ. Heavy metal toxicity and the environment. Exs 2012; 101: 133-164.

[64] Shen S, Li XF, Cullen WR, Weinfeld M and Le XC. Arsenic binding to proteins. Chem Rev 2013; 113: 7769-7792.

[65] Munro KL, Mariana A, Klavins AI, Foster AJ, Lai B, Vogt S, Cai Z, Harris HH and Dillon CT. Microprobe XRF mapping and XAS investigations of the intracellular metabolism of arsenic for understanding arsenic-induced toxicity. Chem Res Toxicol 2008; 21: 1760-1769.

[66] Andrahennadi R and Pickering IJ. Arsenic accumulation, biotransformation and localisation in bertha armyworm moths. Envir Chem 2008; 5: 413-419.

[67] Rubio M, Perez RD, Perez CA, Eynard AH and Bongiovanni GA. Synchrotron microscopic X-ray fluorescence analysis of the effects of chronic arsenic exposure in rat brain. Radiat Phys Chem 2008; 77: 1-8.

[68] Burns FJ, Rossman T, Vega K, Uddin A, Vogt S, Lai B and Reeder RJ. Mechanism of selenium-induced inhibition of arsenic-enhanced UVR carcinogenesis in mice. Environ Health Persp 2008; 116: 703-708.

[69] Kempson IM and Henry DA. Determination of arsenic poisoning and metabolism in hair by synchrotron radiation: the case of Phar Lap. Angew Chem Int Ed 2010; 49: 4237-4240.

[70] Cui G, Ye Z, Zhang R, Wang G and Yuan J. Design and synthesis of a terbium(III) complex-based luminescence probe for time-gated luminescence detection of mercury(II) Ions. J Fluoresc 2012; 22: 261-267.

[71] Zahir F, Rizwi SJ, Haq SK and Khan RH. Low dose mercury toxicity and human health. Environ Toxicol Pharmacol 2005; 20: 351-360.

[72] Korbas M, Blechinger SR, Krone PH, Pickering IJ and George GN. Localizing organomercury

uptake and accumulation in zebrafish larvae at the tissue and cellular level. Proc Natl Acad Sci U S A 2008; 105: 12108-12112.

[73] Korbas M, Krone PH, Pickering IJ and George GN. Dynamic accumulation and redistribution of methylmercury in the lens of developing zebrafish embryos and larvae. J Biol Inorg Chem 2010; 15: 1137-1145.

[74] Korbas M, MacDonald TC, Pickering IJ, George GN and Krone PH. Chemical form matters: differential accumulation of mercury following inorganic and organic mercury exposures in Zebrafish larvae. ACS Chem Biol 2012; 7: 411-420.

[75] Korbas M, Lai B, Vogt S, Gleber SC, Karunakaran C, Pickering IJ, Krone PH and George GN. Methylmercury targets photoreceptor outer segments. ACS Chem Biol 2013; 8: 2256-2263.

[76] MacDonald TC, Nehzati S, Sylvain NJ, James AK, Korbas M, Caine S, Pickering IJ, George GN and Krone PH. Phenylthiourea alters toxicity of mercury compounds in zebrafish larvae. J Inorg Biochem 2015; 151: 10-17.

[77] Choudhury S, Thomas JK, Sylvain NJ, Ponomarenko O, Gordon RA, Heald SM, Janz DM, Krone PH, Coulthard I, George GN and Pickering IJ. Selenium preferentially accumulates in the eye lens following embryonic exposure: a confocal X-ray fluorescence imaging study. Environ Sci Technol 2015; 49: 2255-2261.

[78] Korbas M, O'Donoghue JL, Watson GE, Pickering IJ, Singh SP, Myers GJ, Clarkson TW and George GN. The chemical nature of mercury in human brain following poisoning or environmental exposure. ACS Chem Neurosci 2010; 1: 810-818.

[79] MacDonald TC, Korbas M, James AK, Sylvain NJ, Hackett MJ, Nehzati S, Krone PH, George GN and Pickering IJ. Interaction of mercury and selenium in the larval stage zebrafish vertebrate model. Metallomics 2015; 7: 1247-1255.

[80] Harris HH, Vogt S, Eastgate H, Legnini DG, Hornberger B, Cai Z, Lai B and Lay PA. Migration of mercury from dental amalgam through human teeth. J Synchrotron Radiat 2008; 15: 123-128.

[81] Swanston T, Varney T, Coulthard I, George GN, Pickering IJ, Murphy R and Cooper DM. Synchrotron X-ray fluorescence imaging evidence of biogenic mercury identified in a burial in colonial Antigua. J Archaeol Sci 2015; 58: 26-30.

[82] Wittmers LE, Wallgren J, Alich A, Aufderheide AC and Rapp G. Lead in Bone. IV. distribution of lead in the human skeleton. Arch Environ Health 1988; 43: 381-391.

[83] Zoeger N, Roschger P, Hofstaetter JG, Jokubonis C, Pepponi G, Falkenberg G, Fratzl P, Berzlanovich A, Osterode W, Streli C and Wobraus-

chek P. Lead accumulation in tidemark of articular cartilage. Osteoarthr Cartil 2006; 14: 906-913.

[84] Roschger A, Hofstaetter JG, Pemmer B, Zoeger N, Wobrauschek P, Falkenberg G, Simon R, Berzlanovich A, Thaler HW, Roschger P, Klaushofer K and Streli C. Differential accumulation of lead and zinc in double-tidemarks of articular cartilage. Osteoarthr Cartil 2013; 21: 1707-1715.

[85] Zoeger N, Streli C, Wobrauschek P, Jokubonis C, Pepponi G, Roschger P, Hofstaetter J, Berzlanovich A, Wegrzynek D, Chinea-Cano E, Markowicz A, Simon R and Falkenberg G. Determination of the elemental distribution in human joint bones by SR micro XRF. X-Ray Spectrom 2008; 37: 3-11.

[86] Pemmer B, Roschger A, Wastl A, Hofstaetter JG, Wobrauschek P, Simon R, Thaler HW, Roschger P, Klaushofer K and Streli C. Spatial distribution of the trace elements zinc, strontium and lead in human bone tissue. Bone 2013; 57: 184-193.

[87] Zoeger N, Wobrauschek P, Streli C, Pepponi G, Roschger P, Falkenberg G and Osterode W. Distribution of Pb and Zn in slices of human bone by synchrotron μ-XRF. X-Ray Spectrom 2005; 34: 140-143.

[88] Bellis DJ, Li D, Chen Z, Gibson WM and Parsons PJ. Measurement of the microdistribution of strontium and lead in bone via benchtop monochromatic microbeam X-ray fluorescence with a low power source. J Anal Atom Spectrom 2009; 24: 622-626.

[89] Arora M, Kennedy BJ, Ryan CG, Boadle RA, Walker DM, Harland CL, Lai B, Cai Z, Vogt S, Zoellner H and Chan SWY. The application of synchrotron radiation induced X-ray emission in the measurement of zinc and lead in Wistar rat ameloblasts. Arch Oral Biol 2007; 52: 938-944.

[90] Lanzirotti A, Bianucci R, LeGeros R, Bromage TG, Giuffra V, Ferroglio E, Fornaciari G and Appenzeller O. Assessing heavy metal exposure in Renaissance Europe using synchrotron microbeam techniques. J Archaeol Sci 2014; 52: 204-217.

[91] Lison D, De Boeck M, Verougstraete V and Kirsch-Volders M. Update on the genotoxicity and carcinogenicity of cobalt compounds. Occup Environ Med 2001; 58: 619-625.

[92] Leonardo T, Farhi E, Boisson AM, Vial J, Cloetens P, Bohic S and Rivasseau C. Determination of elemental distribution in green microalgae using synchrotron radiation nano X-ray fluorescence (SR-nXRF) and electron microscopy techniques - subcellular localization and quantitative imaging of silver and cobalt uptake by coccomyxa actinabiotis. Metallomics 2014; 6: 316-329.

[93] Ortega R, Bresson C, Fraysse A, Sandre C, Devès G, Gombert C, Tabarant M, Bleuet P, Seznec H, Simionovici A, Moretto P and Moulin C. Cobalt distribution in keratinocyte cells indicates nuclear and perinuclear accumulation and interaction with magnesium and zinc homeostasis. Toxicol Lett 2009; 188: 26-32.

[94] Zhitkovich A. Chromium in drinking water: sources, metabolism, and cancer risks. Chem Res Toxicol 2011; 24: 1617-1629.

[95] Kemner KM, Kelly SD, Lai B, Maser J, O'Loughlin EJ, Sholto-Douglas D, Cai Z, Schneegurt MA, Kulpa CF and Nealson KH. Elemental and redox analysis of single bacterial cells by X-ray microbeam analysis. Science 2004; 306: 686-687.

[96] Ortega R, Fayard B, Salomé M, Devès G and Susini J. Chromium oxidation state mapping in human cells. J Phys IV France 2003; 104: 289-292.

[97] Ortega R, Fayard B, Salomé M, Devès G and Susini J. Chromium oxidation state imaging in mammalian cells exposed in vitro to soluble or particulate chromate compounds. Chem Res Toxicol 2005; 18: 1512-1519.

[98] Dillon C, Lay P, Kennedy B, Stampfl A, Cai Z, Ilinski P, Rodrigues W, Legnini D, Lai B and Maser J. Hard X-ray microprobe studies of chromium(VI)-treated V79 Chinese hamster lung cells: intracellular mapping of the biotransformation products of a chromium carcinogen. J Biol Inorg Chem 2002; 7: 640-645.

[99] Harris H, Levina A, Dillon C, Mulyani I, Lai B, Cai Z and Lay P. Time-dependent uptake, distribution and biotransformation of chromium(VI) in individual and bulk human lung cells: application of synchrotron radiation techniques. J Biol Inorg Chem 2005; 10: 105-118.

[100] Durham T and Snow E. Metal ions and carcinogenesis. In: editors. Cancer: cell structures, carcinogens and genomic instability. Birkhäuser Basel; 2006. pp. 97-130.

[101] Tokar EJ, Benbrahim-Tallaa L and Waalkes MP. Metal ions in human cancer development. Met Ions Life Sci 2011; 8: 375-401.

[102] Smith AJ, Dieppe P, Porter M and Blom AW. Risk of cancer in first seven years after metal-on-metal hip replacement compared with other bearings and general population: linkage study between the national joint registry of England and Wales and hospital episode statistics. BMJ 2012; 344: e2383.

[103] Rocha HS, Pereira GR, Anjos MJ, Faria P, Kellermann G, Pérez CA, Tirao G, Mazzaro I, Giles C and Lopes RT. Diffraction enhanced imaging and x-ray fluorescence microtomography for analyzing biological samples. X-Ray Spectrom 2007; 36: 247-253.

[104] Pereira GR, Rocha HS, Anjos MJ, Faria P, Pérez CA and Lopes RT. X-ray fluorescence and X-ray

transmission microtomography imaging system. Nucl Instr Meth Phys Res A 2007; 581: 128-132.

[105] Ortega R, Deves G and Carmona A. Bio-metals imaging and speciation in cells using proton and synchrotron radiation X-ray microspectroscopy. J R Soc Interface 2009; 6 Suppl 5: S649-658.

[106] Farquharson MJ and Geraki K. The use of combined trace element XRF and EDXRD data as a histopathology tool using a multivariate analysis approach in characterizing breast tissue. X-Ray Spectrom 2004; 33: 240-245.

[107] Masami A, Katsuhito Y, Chiho O, Hiroyasu E, Kazuyuki H, Hiroshi S, Gang L, Anton M and Toshiaki K. Attempt at two-dimensional mapping of X-ray fluorescence from breast cancer tissue. Jpn J Appl Phy 2005; 44: L998.

[108] Geraki K, Farquharson MJ and Bradley DA. Concentrations of Fe, Cu and Zn in breast tissue: a synchrotron XRF study. Phys Med Biol 2002; 47: 2327-2339.

[109] Farquharson MJ, Geraki K, Falkenberg G, Leek R and Harris A. The localisation and micromapping of copper and other trace elements in breast tumours using a synchrotron micro-XRF system. Appl Radiat Isot 2007; 65: 183-188.

[110] Pereira GR, Rocha HS, Anjos MJ, Farias PC, Perez CA and Lopes RT. Elemental distribution mapping on breast tissue samples. Eur J Radiol 2008; 68: S104-108.

[111] Farquharson MJ, Al-Ebraheem A, Falkenberg G, Leek R, Harris AL and Bradley DA. The distribution of trace elements Ca, Fe, Cu and Zn and the determination of copper oxidation state in breast tumour tissue using muSRXRF and muXANES. Phys Med Biol 2008; 53: 3023-3037.

[112] Podgórczyk M, Kwiatek WM, Grolimund D and Borca C. Technical aspects of Zn microanalysis of human prostate cancer tissues and cells. Radiation Physics and Chemistry 2009; 78: S53-S57.

[113] Ide-Ektessabi A, Fujisawa S, Sugimura K, Kitamura Y and Gotoh A. Quantitative analysis of zinc in prostate cancer tissues using synchrotron radiation microbeams. X-Ray Spectrom 2002; 31: 7-11.

[114] Leitao RG, Santos CAN, Palumbo A, Souza PAVR, Pereira GR, Anjos MJ, Nasciutti LE and Lopes RT. Distribution of Fe, Cu and Zn in Cellular spheroid derived human prostate tumor cells by synchrotron X-Ray fluorescence. IEEE Trans Nucl Sci 2013; 60: 758-762.

[115] Al-Ebraheem A, Mersov A, Gurusamy K and Farquharson MJ. Distribution of Ca, Fe, Cu and Zn in primary colorectal cancer and secondary colorectal liver metastases. Nucl Instr Meth Phys Res A 2010; 619: 338-343.

[116] Al-Ebraheem A, Farquharson MJ and Ryan E. The evaluation of biologically important trace metals in liver, kidney and breast tissue. Appl Radiat Isot 2009; 67: 470-474.

[117] Finney L, Vogt S, Fukai T and Glesne D. Copper and angiogenesis: unravelling a relationship key to cancer progression. Clin Exp Pharmacol Physiol 2009; 36: 88-94.

[118] Finney L, Mandava S, Ursos L, Zhang W, Rodi D, Vogt S, Legnini D, Maser J, Ikpatt F, Olopade OI and Glesne D. X-ray fluorescence microscopy reveals large-scale relocalization and extracellular translocation of cellular copper during angiogenesis. Proc Natl Acad Sci U S A 2007; 104: 2247-2252.

[119] Collingwood JF and Davidson MR. The role of iron in neurodegenerative disorders: insights and opportunities with synchrotron light. Front Pharmacol 2014; 5: 191-210.

[120] Vogt S and Ralle M. Opportunities in multidimensional trace metal imaging: taking copper-associated disease research to the next level. Anal Bioanal Chem 2013; 405: 1809-1820.

[121] Bourassa MW and Miller LM. Metal imaging in neurodegenerative diseases. Metallomics 2012; 4: 721-738.

[122] Popescu BF and Nichol H. Mapping brain metals to evaluate therapies for neurodegenerative disease. CNS Neurosci Ther 2011; 17: 256-268.

[123] Pushie MJ, Pickering IJ, Martin GR, Tsutsui S, Jirik FR and George GN. Prion protein expression level alters regional copper, iron and zinc content in the mouse brain. Metallomics 2011; 3: 206-214.

[124] Grubman A, James SA, James J, Duncan C, Volitakis I, Hickey JL, Crouch PJ, Donnelly PS, Kanninen KM, Liddell JR, Cotman SL, de Jonge MD and White AR. X-ray fluorescence imaging reveals subcellular biometal disturbances in a childhood neurodegenerative disorder. Chem Sci 2014; 5: 2503-2516.

[125] Daoust A, Barbier EL and Bohic S. Manganese enhanced MRI in rat hippocampus: a correlative study with synchrotron X-ray microprobe. NeuroImage 2013; 64: 10-18.

[126] Robison G, Sullivan B, Cannon JR and Pushkar Y. Identification of dopaminergic neurons of the substantia nigra pars compacta as a target of manganese accumulation. Metallomics 2015; 7: 748-755.

[127] Robison G, Zakharova T, Fu S, Jiang W, Fulper R, Barrea R, Zheng W and Pushkar Y. X-ray fluorescence imaging of the hippocampal formation after manganese exposure. Metallomics 2013; 5: 1554-1565.

[128] Silasi G, Klahr AC, Hackett MJ, Auriat AM, Nichol H and Colbourne F. Prolonged therapeutic hypothermia does not adversely impact neuro-

plasticity after global ischemia in rats. J Cereb Blood Flow Metab 2012; 32: 1525-1534.

[129] Chwiej J, Dulinska J, Janeczko K, Appel K and Setkowicz Z. Variations in elemental compositions of rat hippocampal formation between acute and latent phases of pilocarpine-induced epilepsy: an X-ray fluorescence microscopy study. J Biol Inorg Chem 2012; 17: 731-739.

[130] Chwiej J, Sarapata A, Janeczko K, Stegowski Z, Appel K and Setkowicz Z. X-ray fluorescence analysis of long-term changes in the levels and distributions of trace elements in the rat brain following mechanical injury. J Biol Inorg Chem 2011; 16: 275-283.

[131] Chwiej J, Kutorasinska J, Janeczko K, Gzielo-Jurek K, Uram L, Appel K, Simon R and Setkowicz Z. Progress of elemental anomalies of hippocampal formation in the pilocarpine model of temporal lobe epilepsy--an X-ray fluorescence microscopy study. Anal Bioanal Chem 2012; 404: 3071-3080.

[132] Chwiej J, Winiarski W, Ciarach M, Janeczko K, Lankosz M, Rickers K and Setkowicz Z. The role of trace elements in the pathogenesis and progress of pilocarpine-induced epileptic seizures. J Biol Inorg Chem 2008; 13: 1267-1274.

[133] Kumar A, Singh A and Ekavali. A review on Alzheimer's disease pathophysiology and its management: an update. Pharmacol Rep 2015; 67: 195-203.

[134] Huang Y and Mucke L. Alzheimer mechanisms and therapeutic strategies. Cell 2012; 148: 1204-1222.

[135] Braidy N, Poljak A, Marjo C, Rutlidge H, Rich A, Jayasena T, Inestrosa NC and Sachdev P. Metal and complementary molecular bioimaging in Alzheimer's disease. Front Aging Neurosc 2014; 6: 138.

[136] Wang HJ, Wang M, Wang B, Meng XY, Wang Y, Li M, Feng WY, Zhao YL and Chai ZF. Quantitative imaging of element spatial distribution in the brain section of a mouse model of Alzheimer's disease using synchrotron radiation X-ray fluorescence analysis. J Anal Atomic Spectrom 2010; 25: 328-333.

[137] Leskovjan AC, Lanzirotti A and Miller LM. Amyloid plaques in PSAPP mice bind less metal than plaques in human Alzheimer's disease. NeuroImage 2009; 47: 1215-1220.

[138] Leskovjan AC, Kretlow A, Lanzirotti A, Barrea R, Vogt S and Miller LM. Increased brain iron coincides with early plaque formation in a mouse model of Alzheimer's disease. NeuroImage 2011; 55: 32-38.

[139] Wang H, Wang M, Wang B, Li M, Chen H, Yu X, Zhao Y, Feng W and Chai Z. The distribution profile and oxidation states of biometals in APP transgenic mouse brain: dyshomeostasis

with age and as a function of the development of Alzheimer's disease. Metallomics 2012; 4: 289-296.

[140] Adlard PA, Parncutt J, Lal V, James S, Hare D, Doble P, Finkelstein DI and Bush AI. Metal chaperones prevent zinc-mediated cognitive decline. Neurobiol Dis 2015; 81: 196-202.

[141] Politis M. Neuroimaging in Parkinson disease: from research setting to clinical practice. Nat Rev Neurol 2014; 10: 708-722.

[142] Connolly BS and Lang AE. Pharmacological treatment of parkinson disease: a review. JAMA 2014; 311: 1670-1683.

[143] Davie CA. A review of Parkinson's disease. Br Med Bull 2008; 86: 109-127.

[144] Bogdan FG, Martin JG, Uwe B, Alex VG, Michael EK, Richard PE, Katharina L, Richard MD, Graham NG, Akela DH, Sheri MH, Chapman LD, Ingrid JP and Helen N. Mapping metals in Parkinson's and normal brain using rapid-scanning x-ray fluorescence. Phys Med Biol 2009; 54: 651.

[145] Chwiej J. The use of cluster and discriminant analysis in the investigations of the role of trace metals in the pathogenesis of Parkinson's disease. J Trace Elem Med Biol 2010; 24: 78-88.

[146] Davies KM, Bohic S, Carmona A, Ortega R, Cottam V, Hare DJ, Finberg JP, Reyes S, Halliday GM, Mercer JF and Double KL. Copper pathology in vulnerable brain regions in Parkinson's disease. Neurobiol Aging 2014; 35: 858-866.

[147] Robison G, Zakharova T, Fu S, Jiang W, Fulper R, Barrea R, Marcus MA, Zheng W and Pushkar Y. X-Ray fluorescence imaging: a new tool for studying manganese neurotoxicity. PLoS One 2012; 7: e48899.

[148] Dučić T, Barski E, Salome M, Koch JC, Bähr M and Lingor P. X-ray fluorescence analysis of iron and manganese distribution in primary dopaminergic neurons. J Neurochem 2013; 124: 250-261.

[149] Carmona A, Devès G, Roudeau S, Cloetens P, Bohic S and Ortega R. Manganese accumulates within golgi apparatus in dopaminergic cells as revealed by synchrotron X-ray fluorescence nanoimaging. ACS Chem Neurosci 2010; 1: 194-203.

[150] Jung C, Kaul MG, Bruns OT, Ducic T, Freund B, Heine M, Reimer R, Meents A, Salmen SC, Weller H, Nielsen P, Adam G, Heeren J and Ittrich H. Intraperitoneal injection improves the uptake of nanoparticle-labeled high-density lipoprotein to atherosclerotic plaques compared with intravenous injection: a multimodal imaging study in ApoE knockout mice. Circ Cardiovasc Imaging 2014; 7: 303-311.

[151] House MJ, Fleming AJ, de Jonge MD, Paterson D, Howard DL, Carpenter JP, Pennell DJ and St Pierre TG. Mapping iron in human heart tissue

with synchrotron x-ray fluorescence microscopy and cardiovascular magnetic resonance. J Cardiovasc Magn Reson 2014; 16: 80.

[152] Witting PK, Harris HH, Rayner BS, Aitken JB, Dillon CT, Stocker R, Lai B, Cai Z and Lay PA. The endothelium-derived hyperpolarizing factor, H_2O_2, promotes metal-ion efflux in aortic endothelial cells: elemental mapping by a hard X-ray microprobe. Biochem 2006; 45: 12500-12509.

[153] Silva ALM, Figueroa R, Jaramillo A, Carvalho ML and Veloso JF. Performance of a gaseous detector based energy dispersive X-ray fluorescence imaging system: analysis of human teeth treated with dental amalgam. Spectrochim Acta B 2013; 86: 115-122.

[154] Harris H, Vogt S, Eastgate H and Lay P. A link between copper and dental caries in human teeth identified by X-ray fluorescence elemental mapping. J BiolInorg Chem 2008; 13: 303-306.